Journal of Membrane Science 471 (2014) 130–137

Contents lists available at ScienceDirect

Journal of Membrane Science

journal homepage: www.elsevier.com/locate/memsci

Effect of fouling layer spatial distribution on permeate flux: A theoretical and experimental study

K.J. Martin [a,1], D. Bolster [a], N. Derlon [b], E. Morgenroth [b,c], R. Nerenberg [a,*]

[a] Department of Civil and Environmental Engineering and Earth Sciences, University of Notre Dame, 156 Fitzpatrick Hall, Notre Dame, IN 46556, USA
[b] Eawag: Swiss Federal Institute of Aquatic Science and Technology, Überlandstrasse 133, CH-8600 Dübendorf, Switzerland
[c] Institute of Environmental Engineering, ETH Zürich, CH-8093 Zürich, Switzerland

ARTICLE INFO

Article history:
Received 3 February 2014
Received in revised form
31 May 2014
Accepted 21 July 2014
Available online 12 August 2014

Keywords:
Fouling
Gravity driven membrane;
Ultrafiltration
Hydraulic resistance;
Membrane
Optical coherence tomography

ABSTRACT

Fouling layers developing on membrane filters can display significant spatial heterogeneity (roughness), yet the effect of fouling layer spatial distribution on hydraulic resistance has not been studied systematically. We used simple flux models, based on Darcy's law, to assess the impact of spatial distribution on resistance and permeate flux. Our results show that, for a given mean fouling layer thickness, greater spatial heterogeneity could increase fluxes by over an order of magnitude. The degree of error depended on the membrane resistance, fouling layer permeability, and the characteristics of the spatial distribution. We developed 1-dimensional and 2-dimensional flow models, both considering spatial heterogeneity, to improve the accuracy of the conventional model. The proposed models were validated with experimental data from a gravity driven membrane filter with a fouling layer having a high degree of spatial heterogeneity. Accounting for spatial heterogeneity significantly improved the prediction of permeate flux.

1. Introduction

Fouling is a major concern for membrane filtration systems, as it leads to reduced permeate flux, increased energy demand, higher chemical cost, and decreased membrane life [1–4]. A common fouling mechanism is the development of a fouling layer, also known as a cake, on the membrane surface [5–7]. Depending on the application, the fouling layer may consist of primarily inorganic particles (e.g., scale), primarily organic particles (e.g., bacteria, biological flocs, biopolymers), or a combination of both.

For a given filtration system, it is common to correlate fouling layer thickness, total mass, or total volume with hydraulic resistance and permeate flux. However, the impact of the fouling layer on flux is not solely a function of mean thickness, mass, or volume, but also of the spatial distribution of the fouling material or biofilm across the membrane surface. Having a heterogeneous spatial distribution (i.e., uneven distribution) has been shown to significantly impact the flux in recent experimental research [8].

Most research implicitly assumes the fouling layer is one-dimensional (1-d) (i.e., smooth). However, fouling layers can display significant spatial heterogeneity, which commonly is quantified by relative roughness *r*. Hwang at al. [9] reported fouling layer *r* values between 0.37 and 0.66 for a membrane bioreactor (MBR), and Derlon et al. [8] found *r* values between 0.1 and 0.8 for an ultra-low-pressure ultrafiltration (UF) membrane system. For reference, an *r* of zero is a flat surface and increasing *r* values represent a progressively rougher surface. Others have studied the heterogeneity of inorganic, particulate fouling layers, but did not describe the fouling layers in terms of roughness [10].

Recent multidimensional modeling research has simulated heterogeneous fouling layer morphologies that develop in systems with complex hydrodynamics. For example, Picioreanu et al. [11] and Vrouwenvelder et al. [12] assessed fouling of reverse osmosis (RO) membranes in a cross-flow, spiral-wound membrane configuration with a membrane spacer net. Using sophisticated three-dimensional (3-d) biofilm modeling and advanced experimental measurement techniques, they demonstrated significant spatial variation in fouling layer thicknesses. Shin et al. [13] developed a three-dimensional model predicting the development of a particulate fouling layer, and also found that non-uniform fouling layer thicknesses were obtained. However, neither study assessed the effect of surface heterogeneity on permeate flux in a systematic fashion.

The objective of this research was to theoretically and experimentally assess the impact of fouling layer spatial heterogeneity on permeate flux. We took a stepwise approach. First, we explored the behavior of the conventional one-dimensional model for flux,

* Corresponding author.
E-mail address: Nerenberg.1@nd.edu (R. Nerenberg).
[1] Current address: Department of Civil and Environmental Engineering, University of Michigan, 1351 Beal Avenue, Ann Arbor, MI 48109, USA.

http://dx.doi.org/10.1016/j.memsci.2014.07.045
0376-7388/

based on a mean fouling layer thickness ("Mean Model"). This was used as a baseline. Then we adapted the Mean Model to include the effects of spatial heterogeneity, but neglect the effects of two-dimensional flow ("1-d Flow Model"). This model was used to develop the concept of equivalent thickness, and determine when spatial heterogeneity is likely to have significant impact. We then compared the simplified, one-dimensional flow model with a fully two-dimensional model ("2-d Flow Model"), where spatial heterogeneity and two-dimensional flows were included. Finally, we compared the three models for their ability to predict fluxes in a gravity driven membrane (GDM) filtration system where fluxes and spatial heterogeneity were monitored over time.

2. Methods

2.1. Basic flux model

The most common model for predicting permeate flux $J[\mathrm{L\,m^{-2}\,h^{-1}}]$ in membrane filtration is based on Darcy's Law, assuming resistances in-series [5],

$$J=\frac{\Delta P}{\mu R_T}=\frac{\Delta P}{\mu\,(R_m+R_f)} \tag{1}$$

where ΔP [mbar] is the total hydraulic pressure drop across the membrane and fouling layer, μ [mbar s] is the dynamic viscosity of the permeate, and R_T [$\mathrm{m^{-1}}$] is the total hydraulic resistance. In this study, R_T only includes membrane resistance R_m [$\mathrm{m^{-1}}$] and fouling layer resistance R_f [$\mathrm{m^{-1}}$], so that $R_T=R_m+R_f$. We neglect other common types of flux resistance, such as irreversible fouling and concentration polarization, to simplify the model and focus on the effects of the fouling layer. In recent literature, osmotic pressure in biofouling layers has also been identified as a major fouling mechanism: negatively charged functional groups of the extracellular polymeric substance (EPS) and soluble microbial products (SMPs) cause high concentrations of counter-ions to reside within the pores of the fouling layer for reasons of electro-neutrality [14,15]. We do not explicitly account for osmotic pressure, though roughly, its effect on resistance is implicitly included in our estimation of R_f. Note that concentration polarization is not a concern for the GDM case study, which is based on freshwater filtration through UF membranes (see Section 2.3).

Fouling layer resistance R_f is assumed to be proportional to the fouling layer thickness L_f [m] and inversely proportional to the fouling layer permeability κ_f [$\mathrm{m^2}$] [5,16],

$$R_f=\frac{L_f}{\kappa_f} \tag{2}$$

The maximum or clean membrane flux, J^o, occurs when $L_f=0$. For this situation, $R_T=R_m$. Therefore,

$$J^o=\frac{\Delta P}{\mu\,(R_m)} \tag{3}$$

The dimensionless (i.e., normalized) flux J^* is defined as the ratio of the actual flux and the maximum flux,

$$J^*=\frac{J}{J^o}=\frac{R_m}{(R_m+R_f)} \tag{4}$$

Expressing the flux in its dimensionless form allows for evaluation of flux behavior independent of ΔP and μ. Substituting Eq. (2) into Eq. (4),

$$J^*=\frac{R_m}{(R_m+(L_f/\kappa_f))} \tag{5}$$

In order to make Eq. (5) independent of membrane resistance and fouling layer permeability, we define dimensionless fouling layer thickness L_f^* as

$$L_f^*=\frac{L_f}{L_{f50}} \tag{6}$$

where L_{f50} (μm) is the fouling layer thickness that, for a given membrane resistance R_m and fouling layer permeability κ_f, makes the flux equal to half of its maximum value (i.e., that makes J^* equal to 0.5). From Eq. (5), it can be seen that,

$$L_{f50}=R_m\kappa_f \tag{7}$$

Substituting Eq. (7) into Eq. (5),

$$J^*=\frac{1}{(1+L_f^*)} \tag{8}$$

2.2. GDM Flux Models

The next three models, each based on Darcy's Law, take different approaches to represent fouling layer thickness and permeate flow dimensionality. The three models were used to simulate the flux for fouling layers captured in the case study.

2.2.1. Mean Model

The Mean Model only considers the arithmetic mean thickness of the fouling layer. Assuming a 2-d fouling layer, we can define an interval of width Δx and calculate the arithmetic mean thickness $L_{f,mean}$ and $L_{f\,mean}^*$ for a thickness data set consisting of n points (Fig. 1),

$$L_{f,mean}=\frac{1}{n}\sum_{i=1}^{n}L_{fi} \tag{9}$$

$$L_{f,mean}^*=\frac{1}{n}\left(\sum_{i=1}^{n}L_{fi}\right)L_{f,50}^{-1} \tag{10}$$

To solve for permeate flux, $L_{f,mean}$ and $L_{f\,mean}^*$ are substituted into L_f and L_f^* in the basic flux model, Eqs. (1) and (2) and Eq. (8), respectively.

2.2.2. One-dimensional flow model

When the flow is primarily perpendicular to the membrane, it can be modeled as 1-d. For 1-d flow in a structurally heterogeneous fouling layer, permeate flux can be determined by integrating flux across the membrane. A more practical approach is to divide the membrane and fouling layer into n finite segments, assumed to have constant thickness, and average the flux of the n segments (Fig. 1). Alternatively, an equivalent thickness $L_{f,eq}$, the thickness of a uniform fouling layer that provides the same resistance as a rough layer, can be used in the basic flux equation (Eqs. 1 and 2). Equivalent thickness $L_{f,eq}$ is determined by,

$$L_{f,eq}=\left(\frac{1}{\kappa_f n}\sum_{i=1}^{n}\left(R_m+\frac{L_{f_i}}{\kappa_f}\right)^{-1}\right)^{-1}-\kappa_f R_m \tag{11}$$

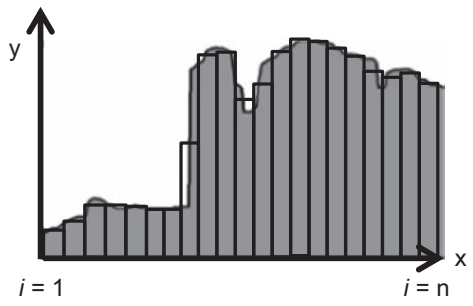

Fig. 1. An example section of fouling layer, divided into finite segments with uniform width.

In cases where membrane resistance R_m is negligible compared to the resistance of the fouling layer R_f, Eq. (11) simplifies to,

$$L_{f,eq} = \left(\frac{1}{n} \sum_{i=1}^{n} (L_{f_i})^{-1} \right)^{-1} \tag{12}$$

In terms of dimensionless L_f^*, Eq. (11) becomes,

$$L_{f\ eq}^* = \left(\frac{1}{n} \sum_{i=1}^{n} (1+L_{f_i}^*)^{-1} \right)^{-1} - 1 \tag{13}$$

Spatial heterogeneity can be assessed by relative roughness, a parameter commonly used to assess the shape or geometry of a biofilm. Relative roughness r is a dimensionless parameter that indicates thickness variability, normalized to the arithmetic mean thickness $L_{f,mean}$ [17–19],

$$r = \frac{1}{n} \sum_{i=1}^{n} \frac{|L_{f_i} - L_{f,mean}|}{L_{f,mean}} \tag{14}$$

2.2.3. Two-dimensional flow model

In order to assess both the effects of spatial heterogeneity and two-dimensional flows in the fouling layer, finite element analysis (FEA) can be used to solve the 2-d steady-state incompressible Darcy equation,

$$\mathbf{u} = -\frac{\kappa}{\mu} \nabla P \tag{15}$$

where $\mathbf{u}$ is the Darcy velocity vector, which consists of the x component, u, and y component, v. For incompressible flow, the velocity field is divergence free such that $(\nabla \mathbf{u}) = 0$.

For a given fouling layer morphology, the top boundary of the fouling layer Γ_f is designated as an inlet with constant pressure $P(\Gamma_f) = H$. To avoid having to geometrically represent the membrane layer in the FEA analysis, we accounted for the impact of the membrane resistance on flux by assigning a velocity term at the fouling layer/membrane interface Γ_m. The velocity term is obtained from the basic flux equation,

$$J(x) = v(x) = \frac{P(\Gamma_m)}{\mu(R_m)} \tag{16}$$

where $P(\Gamma_m)$ is local pressure at the interface between the fouling layer and membrane, assuming the pressure at the underside of the membrane is 0. The lateral boundaries of the morphology at $x=0$ and $x=L_x$ are treated as symmetry boundaries.

2.3. Experimental case study

The fouling model was validated using experimental morphologies from a GDM filter, an ultra-low pressure, dead-end, ultrafiltration system. The GDM filtration system is designed as a low energy and low maintenance drinking water treatment option that operates without any external control of the biofouling layer [8,20,21]. Instead, naturally-occurring metazoan predators in the river source water create spatially heterogeneous biofouling structures that enhance flux [22]. Studies focusing on the effects of predation can be found in Derlon et al. [8,22].

2.3.1. Experimental setup

A GDM system, equipped with two parallel membrane modules referred to as Filter 1 and Filter 2, was operated for two months. A schematic representation of the experimental set-up can be found in Derlon et al. [8]. Natural river water (Chriesbach river, Dübendorf, Switzerland) was used as feed water. Eukaryotic predators were responsible for the development of open and heterogeneous biofouling layers [8].

2.3.2. Membrane

Flat sheet polysulfone membrane (Microdyn-NADIR, Germany) with a nominal cutoff of 100 kDa was used. The membrane was stored for 24 h in deionized water prior to measurement of the clean water flux. The deionized water was renewed several times during this period. Membranes were then placed in filtration modules equipped with a cover slide that was suitable for observation by Optical Coherence Tomography (OCT). The membrane surface area for each module was 0.001875 m^2, and the clean membrane flux was experimentally determined as 70 L m^{-2} h^{-1}.

2.3.3. Operation and data collection

Biofouling layers were developed on membrane surfaces for approximately two months. OCT data were collected every three days. The permeate flux was calculated by daily measuring the mass of permeate using a scale (Ohaus Adventure Pro, Pine Brook, NJ, USA).

2.3.4. Optical coherence tomography

OCT (model 930 nm Spectral Domain, Thorlabs GmbH, Dachau, Germany) with a central light source wavelength of 930 nm was used to investigate the mesoscale structure of the biofilm. For image acquisition, filtration modules were disconnected and carefully placed on the OCT stage. Around 20 randomly selected A-Scans (i.e., XZ plane pictures) of 1.5×5 mm^2 were acquired at different time intervals for each filtration module. An example image is provided in Fig. 2a. Image analysis software developed in MATLAB (MathWorks, Natick, US) was used to analyze OCT images [8]. The OCT images were converted to a data set of points along the outer perimeter of the morphology. The fouling layer thickness was recorded at intervals of $\Delta x = 4$ μm along the membrane. This data set, along with the measured permeate fluxes, was then used in the Mean, 1-d Flow, and 2-d Flow Models.

2.4. Model validation

The proposed mathematical framework of the 1-d Flow and 2-d Flow Models was validated using experimental data from the GDM tests described earlier. The Mean Model flux was used as a baseline. For the 1-d Flow Model, $L_{f,eq}$ was calculated according to Eq. (11) using the OCT data sets generated for each fouling layer image. The 2-d fouling layer domain was constructed from the OCT data set by connecting neighboring coordinate points with straight lines. Because of the high spatial resolution of the data set (i.e., $\Delta x = 4$ μm), curved surfaces of the fouling layer were captured and sharp intersections were avoided. On rare occasion, the fouling layer thickness was 0, implying a clean membrane at this location. Here, we assumed the fouling layer thickness to be 1 μm in order to maintain a single, continuous domain. As an example, the fouling layer image captured by OCT shown in Fig. 2a is reconstructed into the modeling domain shown in Fig. 2b.

A MATLAB program was used to load the OCT coordinate data, estimate permeate flux via the Mean, 1-d Flow, and 2-d Flow

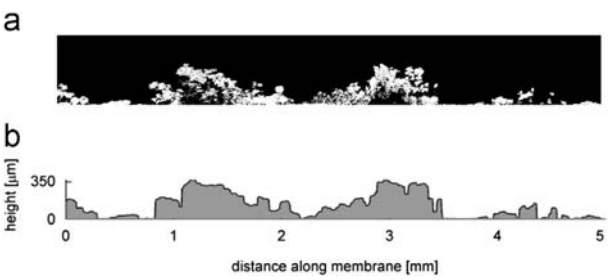

Fig. 2. a) OCT image of an example fouling layer morphology b) 2-d geometry recreated from the OCT data representing the image.

Models, and calculate simple morphological parameters. Solving for 2-d flow in a geometrically complex domain required FEA. MATLAB was coupled with the multiphysics FEA program COMSOL (Comsol 3.5a, Stockholm, Sweden, www.comsol.com) to solve 2-d Darcy's Law. The program was run on one core of a shared dual 6 core 2.4 GHz AMD Opteron Processor with 12 GB of RAM. In roughly 30 min, results were calculated for 20 morphologies.

2.5. Parameters

The parameters required by the models are provided in Table 1. To select a reasonable fouling layer permeability κ_f for use in the simulations of this study, κ_f was back-calculated from the experimental data of the GDM filters. Approximately 12 times over the 40-day GDM experiment, the experimental permeate flux J_{exp} was measured and a set of OCT images collected for each filter. Using the 2-d Flow Model, κ_f was back-calculated from each set of OCT images based on the corresponding J_{exp} measurement. For example, on Day 21, 24 OCT images were taken of the fouling layer morphology of Filter 2. The κ_f value that matched the mean flux of the 24 images with J_{exp} of Filter 2 on Day 21 was determined. The κ_f values, calculated over the life of the experiment, were then averaged to achieve a single value for each filter replicate. Finally, the arithmetic mean of both filter replicates was used in model simulations of this study.

3. Results and discussion

3.1. General impact of fouling layer thickness on flux

Based on Eq. (5), the normalized permeate flux J^* depends on membrane resistance R_m, fouling layer permeability κ_f, and fouling layer thickness L_f. Fig. 3 portrays J^* as a function of L_f for typical microfiltration (MF), UF, nanofiltration (NF) and RO systems assuming membrane resistances of $4\cdot10^{11}$, $7\cdot10^{12}$, $3\cdot10^{13}$, and $3\cdot10^{14}$ m^{-1} [5]. The fouling layer permeability κ_f was assumed to be 10^{-17} m^2 (see Section 3.4.1). As a reminder, the models used in this study do not account for concentration polarization or irreversible fouling.

As shown in Fig. 3a, the sensitivity of J^* to L_f depends on the membrane type. L_f has the greatest impact on membranes with low resistance. A relatively thin fouling layer, on the order of 1–10 μm, can have a significant effect on the total resistance of a MF or UF membrane system, but a small or negligible effect on an NF membrane system.

Fig. 3b displays the relationship of J^* and dimensionless thickness L_f^*, which allows for the impact of fouling layer thickness to be discussed independent of membrane resistance and fouling layer permeability. The sensitivity of J^* to changes in L_f^* is represented by the first derivative, as shown in Fig. 3b (plotted as its negative value). Three arbitrarily defined regions can be identified: high sensitivity, high to low transitional sensitivity, and low sensitivity. For $0<L_f^*<1$, the magnitude of the derivative is high, ranging from -1 to -0.25. This means a change in flux of at least 25% occurs for a unit change in L_f^*. For $1<L_f^*<5$, the slope progressively decreases from -0.25 to -0.03, where the change in J^* becomes as small as 3% for a unit change in L_f^*. For $L_f^*>5$, the slope is even smaller, decreasing from -0.03 to zero, making J^* relatively insensitive to changes in L_f^*. For sake of comparison, based on the assumed values of membrane resistance R_m and fouling layer permeability κ_f, $L_f^*=1$ corresponds to a L_f value of 4 μm for a MF membrane, 75 μm for a UF membrane, 350 μm for a NF membrane, and 3000 μm for a RO membrane.

It may be important to obtain precise measurements of the fouling layer thickness when L_f lies within the region of high sensitivity. For example, for the MF system given in Fig. 3, L_f=40 μm and L_f=50 μm predict J^* values that differ by 20%. In contrast, for these same thicknesses, there is only a difference of 3% in J^* for the NF system.

The second derivative of J^*, plotted in Fig. 3b, indicates the rate of change of the sensitivity of J^* to changes in L_f^*. As seen in the figure, there are also three regions of the slope: high rate of change, transition, and low rate of change. This is discussed further in the next section.

3.2. General comparison of Mean Model and 1-d Flow Model results

Given the nonlinear relationship between J^* and L_f^*, the mean thickness $L_{f\,mean}^*$ of a rough fouling layer may not provide an accurate value of the mean flux J_{mean}^*. For a hypothetical fouling layer where half the layer has a thickness $L_{f\,1}^*=1$ and the other half $L_{f\,2}^*=7$, $L_{f\,mean}^*$ is 4 and the corresponding flux J^* is 0.2 (Fig. 4a). However, the J^* values for $L_{f\,1}^*$ and $L_{f\,2}^*$ are approximately 0.1 and 0.5, respectively, so the actual J_{mean}^* is around 0.3, a value 50% greater than that predicted by the $L_{f\,mean}^*$ (Fig. 4b).

A more accurate approach is to divide the fouling layer into discrete sections, apply the basic flux model to each section, and then average the results to determine J_{mean}^* of the total membrane. When using this "discretized", 1-d approach, an equivalent fouling layer thickness, $L_{f\,eq}^*$, can be determined (Eq. 11). $L_{f\,eq}^*$ is the thickness that results in the J_{mean}^* for the total membrane when used in the conventional Darcy's Law equation. For the example above, $L_{f\,eq}^*=2.3$, which is significantly lower than the $L_{f\,mean}^*$ of 4.

The error associated with using $L_{f\,mean}^*$ rather than $L_{f\,eq}^*$ in the Mean Model depends on the degree of nonlinearity in the flux curve over which the variations in L_f^* take place. This degree of nonlinearity is reflected in the second derivative of J^* with respect to L_f^* (Fig. 3b). The second derivative is greatest at lower values of L_f^*, which means the nonlinearity effect is relevant even when small changes in L_f^* occur in this range. At larger values of L_f^*, the second derivative is much smaller, meaning that greater changes in L_f^* would be needed before the nonlinear effect became significant. In the previous example, with $L_{f\,1}^*=1$ and $L_{f\,2}^*=7$, $\Delta L_f^*=6$ and $L_{f\,mean}^*=4$. In this case, the ratio of $J^*(L_{f\,mean}^*)$:$J^*(L_{f\,eq}^*)$, a measure of the error in using $L_{f\,mean}^*$ to calculate flux, is approximately 0.67, or 33% discrepancy. If $L_{f\,1}^*=4$ and $L_{f\,2}^*=10$,

Table 1
Model parameters.

Parameters		Value	Unit	Source
Dynamic viscosity of water	μ	3.1×10^{-9}	mbar h	[23]
Density of water	P	1000	kg m^{-3}	[23]
Fouling layer hydraulic permeability	κ_f	20×10^{-18}	m^2	Estimated for this study (see Section 3.4.1)
Water pressure exerted on the fouling layer	H	65	mbar	Experimental condition
Membrane resistance	R_m	0.34×10^{12}	m^{-1}	Based on a clean membrane test
Length of each image	L_x	5×10^{-3}	m	Experimental condition
Resolution of y coordinate points in OCT data set	Δx	4×10^{-6}	m	Experimental condition

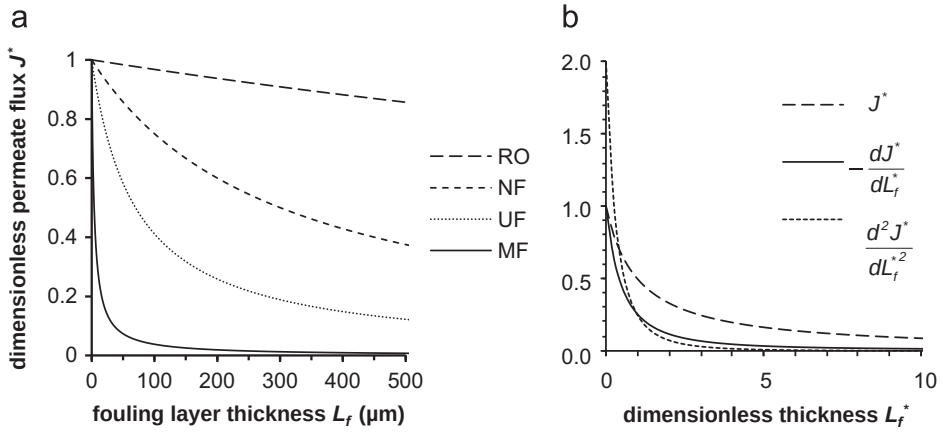

Fig. 3. a) Dimensionless flux J^* as a function of L_f for several types of membrane with a typical fouling layer permeability assumed, and b) J^* as a function of the normalized fouling layer thickness L_f^*, as well as its first and second derivatives with respect to L_f^*.

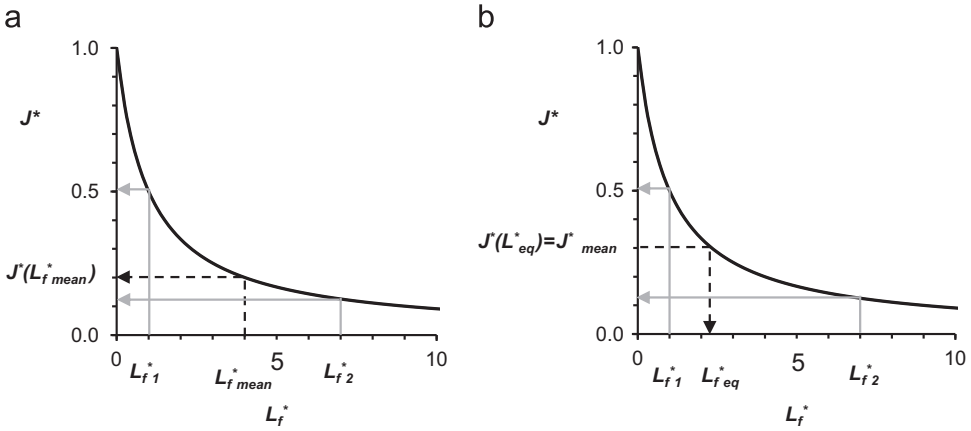

Fig. 4. Illustration of the error in using the mean fouling layer thickness, $L^*_{f\,mean}$, to determine permeate flux J^* for a rough fouling layer. If the fouling layer has two thicknesses, $L^*_{f1}=1$ and $L^*_{f2}=7$, a) the $L^*_{f\,mean}=4$ underestimates the actual $J^*_{mean}=0.3$. b) The actual J^*_{mean} corresponds to an equivalent thickness L^*_{feq} of approximately 2.3.

ΔL_f^* still is 6 but the mean thickness increases to $L^*_{f\,mean}=7$. For this case, $J^*(L^*_{f\,mean})$:$J^*(L^*_{feq})$ is only 0.86, or 14% discrepancy.

The previous examples suggest that the magnitude of the error in using $L^*_{f\,mean}$ to compute flux varies according to: 1) the value of $L^*_{f\,mean}$ and 2) the variation ΔL_f^*. This is illustrated in Fig. 5, where it is assumed there are two fouling layer thicknesses, each comprising half of the fouling layer (Fig. 5a). Fig. 5b plots the ratio of $J^*(L^*_{f\,mean})$:$J^*(L^*_{feq})$. For a given variation in thickness ΔL_f^*, the error in using $L^*_{f\,mean}$ to compute flux is greater for smaller mean thicknesses. This example considers a hypothetical fouling layer with only two thicknesses; a more continuous distribution of thicknesses would have a lesser effect.

Relative roughness r is a parameter commonly used to assess structural heterogeneity of the fouling layers or biofilms by quantifying variations in thickness relative to the arithmetic mean thickness (Eq. 14). As shown in Fig. 6, the relationship between dimensionless flux J^* and r is nonlinear, and the function changes with differing values of $L^*_{f\,mean}$. Hence, while r is a useful parameter to indicate spatial heterogeneity, it is not easily correlated with J^*. Other common parameters, including those assessing total mass and volume of the fouling layer, also disregard spatial heterogeneity, and therefore are poor predictors. The term $(1+L^*_{feq})^{-1}$ has a perfect linear correlation with J^* for any value of $L^*_{f\,mean}$. This is expected since $(1+L^*_{feq})^{-1}$ defines J^* in Eq. (8). In non-dimensionless terms, J correlates with $(R_m+L_{f,eq}/\kappa_f)^{-1}$, and if membrane resistance R_m is negligible compared to fouling layer resistance R_f, J correlates directly with $(L_{f,eq})^{-1}$.

3.3. General comparison of 1-d and 2-d Flow Model results

The 2-d Flow Model captures permeate flow components parallel, as well as perpendicular, to the membrane surface. The error in neglecting 2-d effects may be significant when there are adjacent sections of fouling layer with significant differences in thickness, as depicted in the hypothetical fouling layer in Fig. 7. For this fouling layer, the 2-d Flow Model predicted a flux 30% greater than that of the 1-d Flow Model. Horizontal flow from thin regions to thick regions, especially near the corners connecting the two sections, increases the overall flux. The impact of horizontal flow on the overall flux is highly dependent on the thicknesses of adjacent regions as well as their relative frequency.

2-d effects may also become relevant for morphologies with significant vertical components. Horizontal flow across these boundaries leads to flow interactions uncaptured by the 1-d Flow Model. Furthermore, the 1-d Flow Model does not account for area enlargement, the ratio of the fouling layer perimeter to the membrane length, which increases with vertical boundaries. The impact of these effects on overall flux is highly dependent on the thickness of the fouling layer and local geometry.

Fig. 8 illustrates three fouling layer profiles taken from the GDM case study. Each of the profiles have a mean thickness of 107 ± 3.2 μm, but varying degrees of spatial heterogeneity, expressed as roughness. Using the Mean Model and the parameters described in Table 1, the three profiles have a similar flux, with an average of 3.68 L m^{-2} h^{-1} (Table 2). However, considering

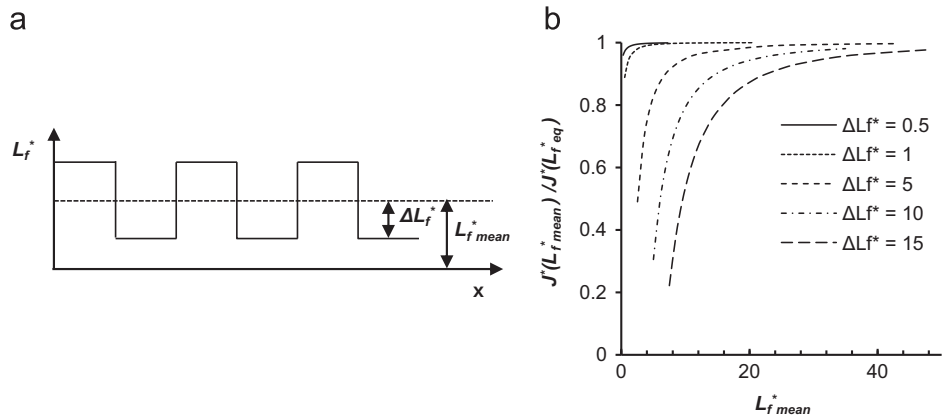

Fig. 5. a) Hypothetical fouling layer morphology, and b) degree of error in using the mean fouling layer thickness to determine permeate flux for the shape depicted in a). A value of $J^*(L_{f\,mean}^*):J^*(L_{f\,eq}^*)=1$ means that $L_{f\,mean}^*$ provides the correct value of J^* when used to calculate flux.

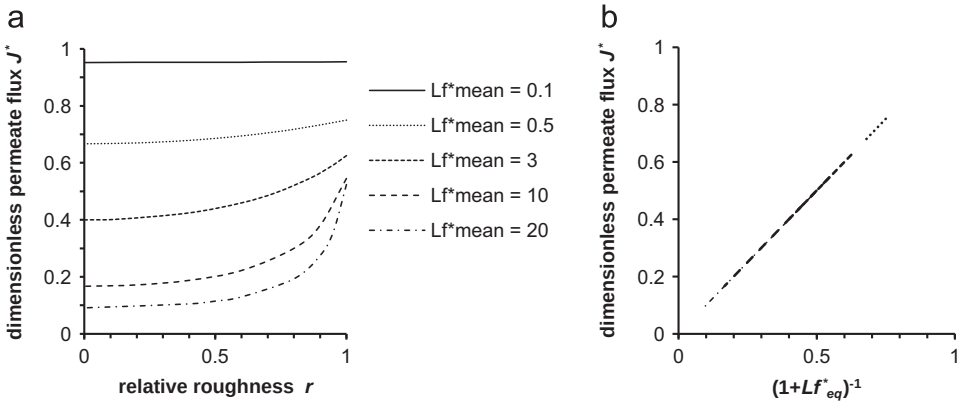

Fig. 6. a) Impact of relative roughness r on dimensionless flux J^* for different mean thickness values, $L_{f\,mean}^*$. Relative roughness has a varying effect on flux, depending on the degree of roughness and the mean thickness. b) The term $(1+L_{f\,eq}^*)^{-1}$ correlates linearly with J^*, and the correlation does not depend on the mean thickness.

the 1-d Flow Model, the fluxes differ significantly, ranging from 4.1 L m^{-2} h^{-1} for profile (a) to 23.2 L m^{-2} h^{-1} for profile (c). The results of the 2-d Flow Model are very similar to the 1-d Flow Model, which suggests that the 1-d Flow Model may be adequate for most situations.

3.4. Experimental case study

3.4.1. Fouling layer permeability

The arithmetic mean fouling layer permeability κ_f, estimated from experimental flux measurements, was determined as $21 \pm 8 \cdot 10^{-18}$ m^2 (see Section 2.5). A value of $\kappa_f = 20 \cdot 10^{-18}$ m^2 was used in the model simulations. For comparison, researchers have found the hydraulic permeability of a bacterial filter cake and an activated sludge cake to be $50 \cdot 10^{-18}$ m^2 and $200 \cdot 10^{-18}$ m^2, respectively [24,25]. Dreszer et al. [26] measured the permeability of biofouling layer developed with synthetic feed water containing sodium acetate. They found the permeability of biofilms to vary between $2 \cdot 10^{-18}$ and $20 \cdot 10^{-18}$ m^2 with the resistance not correlating with layer thickness, but rather applied flux.

3.4.2. Case study results

The three flux models (Mean, 1-d Flow, and 2-d Flow) were compared in their ability to predict the experimental fluxes of a GDM system treating creek water (see Section 2.4). Of the 537 morphologies tested, 75% exhibited less than 10% difference between the 1-d and 2-d-Flow Model flux results, and 92% had a difference below 15%. Over 99% of the morphologies exhibited a difference less than 30%. Thus, for the case study morphologies, the 1-d Flow Model was considered to be sufficiently accurate, especially considering the degree of error introduced by other sources. The 2-d Flow Model results are omitted from Fig. 8 in order to not complicate the plots. Fig. 9 compares the experimental flux J_{exp} with the simulated fluxes of the Mean Model J_{mean} and the 1-d Flow Model J_{1d}.

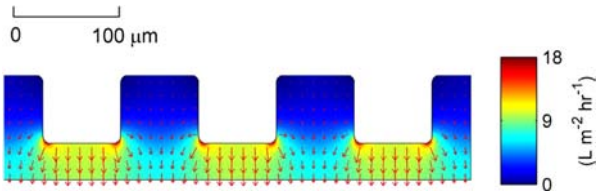

Fig. 7. 2-d permeate flux for an example fouling layer morphology. The surface color represents the magnitude of the permeate flux. The arrows point in the direction of flow and their length indicates the magnitude of the flux.

The mean thickness of the fouling layers generally increased with time (Fig. 9a and b). As a result, the Mean Model predicted a decline in permeate flux with time (Fig. 9c and d). However, this trend was not observed in the experimental fluxes. The 1-d Flow Model better followed the trends of the experimental results. This is especially apparent in Filter 2 between Day 16 and 30: J_{exp} increased despite increasing $L_{f,mean}$ values. By accounting for spatial heterogeneity, the 1-d Flow Model was able to capture the increase in flux. Though relative roughness is not always an appropriate indicator of permeate flux (see Section 3.2), it is

depicted in Fig. 8a and b as a measure of spatial heterogeneity since it can be compared with past studies (see Section 1).

Accounting for spatial heterogeneity improved the flux predictions, yet significant discrepancy between the simulated and experimental results still existed in some cases. The discrepancy may be partially explained by model assumptions, in particular the assumption of constant permeability in space and time. It is plausible the fouling layer permeability changed as the layer aged or was preyed upon [9,18,27]. Predation has been shown to increase porosity which could correspond to an increase in permeability. If this is the case, the models overestimated the first flux measurements and underestimated the flux for the latter test dates. Structural isotropy of the fouling layer is also assumed, while the literature has suggested anisotropy with depth of the fouling layers [9]. Furthermore, the models did not account for hydraulic resistances caused by osmotic pressure, pore-blocking, and irreversible fouling, which may have evolved in time. Varying the ratio of the resistance values would shift and alter the shape of the curves as shown in Fig. 9. In regards to instrument limitation, minor thickness errors in thin regions could have exerted major effect on the calculation of permeate flux, and as the morphologies became more heterogeneous, additional OCT profiles may have been required to correctly represent the fouling layer morphology. Finally, 3-d flow effects were not examined. Nonetheless, despite all the possible sources of error, it is clear that the 1-d Flow Model captured the experimental results better than the Mean Model. Also note that the models used for this analysis neglected factors that may be important for applications other than the GDM filter, such as concentration polarization for RO membranes.

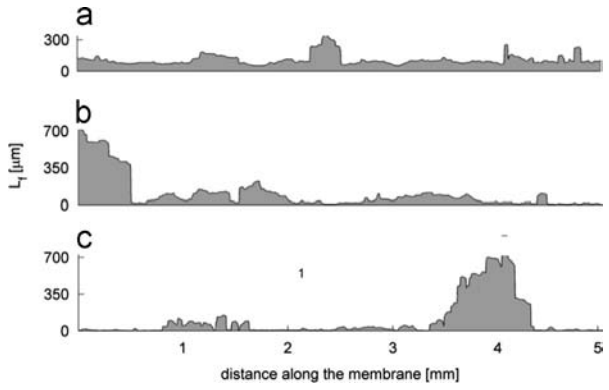

Fig. 8. Fouling layer profiles with similar mean thicknesses of approximately 100 μm, but varying degrees of spatial heterogeneity.

Table 2
Comparison of 1-d and 2-d Flow Model results for fouling layer morphologies.

Profile	Mean thickness (μm)	Relative roughness (−)	Mean Model ($L\,m^{-2}\,h^{-1}$)	1-d Flow Model ($L\,m^{-2}\,h^{-1}$)	2-d Flow Model ($L\,m^{-2}\,h^{-1}$)
a	108	0.31	3.64	4.10	4.35
b	109	0.89	3.61	9.58	10.2
c	103	1.23	3.80	23.2	23.9
Average	107 ± 3.2	0.81 ± 0.47	3.68 ± 0.10	12.3 ± 9.8	12.8 ± 10

This study highlights the significance of fouling layer spatial heterogeneity on hydraulic resistance and, ultimately, permeate flux. Researchers should be mindful of spatial heterogeneity when quantitatively or qualitatively correlating fouling layer thickness, volume, or mass as an indicator of filtration performance. Furthermore, future research should consider the fouling layer spatial heterogeneity when devising fouling mitigation strategies. It may be more beneficial to have a thicker, more heterogeneous fouling layer than a thinner, more uniform one [26]. As an example, the

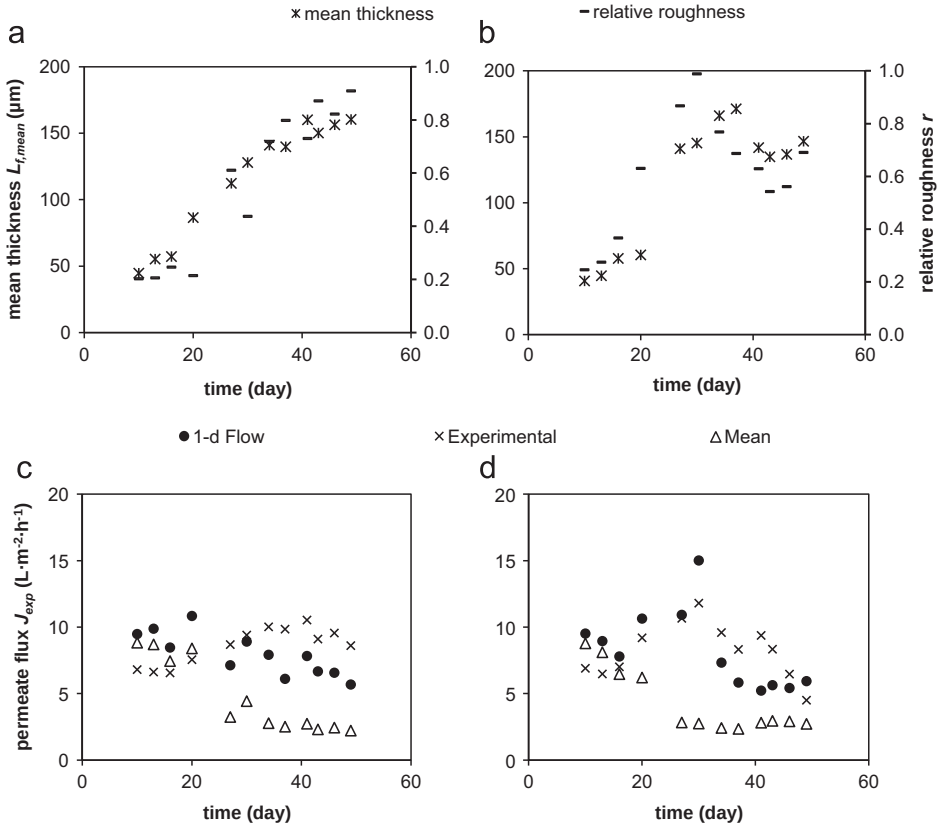

Fig. 9. The mean thickness and relative roughness of a) Filter 1 and b) Filter 2. Comparison of the experimental flux J_{exp} with the flux of the Mean Model J_{mean} and the 1-d Flow Model J_{1d} for the GDM filtration system for c) Filter 1 and d) Filter 2. Filter 1 and Filter 2 were duplicates, operated under identical conditions.

shape of the membrane could be used to manipulate fouling layer morphology. Hashino et al. [28] found gear-shaped hollow fiber membranes to increase relative fouling permeability and recovery by backwashing. The valleys accumulated significant foulant, but the top of the projections remained relatively clean, most likely due to local flow patterns that increased shear stress in these regions.

4. Conclusions

- Fouling layer resistance is dependent not just on the thickness, mass, or volume of the fouling material or biofilm, but also on its spatial distribution.
- Arithmetic mean thickness $L_{f,mean}$ does not lead to accurate permeate fluxes when using a conventional Darcy Law filtration model. For two spatial distributions with the same $L_{f,mean}$, the more heterogeneous distribution will have a higher permeate flux.
- The error in using $L_{f,mean}$ to compute flux is greater when: 1) $L_{f,mean}$ is small, and 2) there exists a high degree of spatial variation in fouling layer thicknesses.
- The impact of fouling layer spatial distribution on permeate flux is not well represented by relative roughness.
- Accounting for spatial distribution in a 1-d Flow Model based on Darcy's Law improved prediction of the permeate flux, especially for fouling layers with highly heterogeneous morphologies.

Acknowledgments

We would like to thank the University of Notre Dame Center for Research Computing for use of the computing cluster, which allowed us to run multiple 2-d simulations simultaneously. K. J. Martin was funded by the University of Notre Dame Center for Environmental Science and Technology Bayer Fellowship and the NSF, United States project CBET0954918 (Nerenberg CAREER award).

References

[1] L.Y. Dudley, J.S. Baker, Biofouling in membrane systems – a review, Desalination 118 (1998) 81–89.
[2] H.C. Flemming, G. Schaule, T. Griebe, J. Schmitt, A. Tamachkiarowa, Biofouling – the Achilles heel of membrane processes, Desalination 113 (1997) 215–225.
[3] K.J. Howe, M.M. Clark, Fouling of microfiltration and ultrafiltration membranes by natural waters, Environ. Sci. Technol. 36 (2002) 3571–3576.
[4] A. Ramesh, D.J. Lee, M.L. Wang, J.P. Hsu, R.S. Juang, K.J. Hwang, J.C. Liu S.J. Tseng, Biofouling in membrane bioreactor, Sep. Sci. Technol. 41 (2006) 1345–1370.
[5] M. Mulder, Basic Priciples of Membrane Technology, Kluwer Academic Publishers, Dordrecht, The Netherlands, 1991.
[6] P. Le-Clech, V. Chen, T.A.G. Fane, Fouling in membrane bioreactors used in wastewater treatment, J. Membr. Sci. 284 (2006) 17–53.
[7] C. Fritzmann, J. Lowenberg, T. Wintgens, T. Melin, State-of-the-art of reverse osmosis desalination, Desalination 216 (2007) 1–76.
[8] N. Derlon, M. Peter-Varbanets, A. Scheidegger, W. Pronk, E. Morgenroth, Predation influences the structure of biofilm developed on ultrafiltration membranes, Water Res. 46 (2012) 3323–3333.
[9] B.K. Hwang, C.H. Lee, I.S. Chang, A. Drews, R. Field, Membrane bioreactor: TMP rise and characterization of bio-cake structure using CLSM-image analysis, J. Membr. Sci. 419 (2012) 33–41.
[10] V.V. Tarabara, F. Pierrisnard, C. Parron, J.Y. Bottero, M.R. Wiesner, Morphology of deposits formed from chemically heterogeneous suspensions: application to membrane filtration, J. Colloid Interface Sci. 256 (2002) 367–377.
[11] C. Picioreanu, J.S. Vrouwenvelder, M.C.M. van Loosdrecht, Three-dimensional modeling of biofouling and fluid dynamics in feed spacer channels of membrane devices, J. Membr. Sci. 345 (2009) 340–354.
[12] J.S. Vrouwenvelder, J. Buiter, M. Riviere, W.G.J. van der Meer, M.C.M. van Loosdrecht, J.C. Kruithof, Impact of flow regime on pressure drop increase and biomass accumulation and morphology in membrane systems, Water Res. 44 (2010) 689–702.
[13] J. Shin, K. Kim, J. Kim, S. Lee, Development of a numerical model for cake layer formation on a membrane, Desalination 309 (2013) 213–221.
[14] H. Lin, M. Zhang, F. Wang, Y. He, J. Chen, H. Hong, A. Wang, H. Yu, Experimental evidence for osmotic pressure-induced fouling in a membrane bioreactor, Bioresour. Technol. 158 (2014) 119–126.
[15] M. Zhang, W. Peng, J. Chen, Y. He, L. Ding, A. Wang, H. Lin, H. Hong, Y. Zhang, H. Yu, A new insight into membrane fouling mechanism in submerged membrane bioreactor: osmotic pressure during cake layer filtration, Water Res. 47 (2013) 2777–2786.
[16] J. Kim, F.A. DiGiano, Fouling models for low-pressure membrane systems, Sep. Purif. Technol. 68 (2009) 293–304.
[17] C. Picioreanu, M.C.M. van Loosdrecht, J.J. Heijnen, A theoretical study on the effect of surface roughness on mass transport and transformation in biofilms, Biotechnol. Bioeng. 68 (2000) 355–369.
[18] R. Murga, P.S. Stewart, D. Daly, Quantitative analysis of biofilm thickness variability, Biotechnol. Bioeng. 45 (1995) 503–510.
[19] A. Heydorn, A. Toftgaard Nielsen, M. Hentzer, C. Sternberg, M. Givskov, B. Kjaer Ersboll, S. Molin, Quantification of biofilm structures by the novel computer program COMSTAT, Microbiology 146 (2000) 2395–2407.
[20] M. Peter-Varbanets, W. Gujer, W. Pronk, Intermittent operation of ultra-low pressure ultrafiltration for decentralized drinking water treatment, Water Res. 46 (2012) 3272–3282.
[21] M. Peter-Varbanets, C. Zurbrugg, C. Swartz, W. Pronk, Decentralized systems for potable water and the potential of membrane technology, Water Res. 43 (2009) 245–265.
[22] N. Derlon, N. Koch, B. Eugster, T. Posch, J. Pernthaler, W. Pronk, E. Morgenroth, Activity of metazoa governs biofilm structure formation and enhances permeate flux during Gravity-Driven Membrane (GDM) filtration, Water Res. 47 (2013) 2085–2095.
[23] W.M. Haynes, CRC Handbook of Chemistry and Physics, CRC Press/Taylor and Francis, Boca Raton, FL, 2012.
[24] R. McDonogh, G. Schaule, H.-C. Flemming, The permeability of biofouling layers on membranes, J. Membr. Sci. 87 (1994) 199–217.
[25] P.S. Stewart, Mini-review: convection around biofilms, Biofouling 28 (2012) 187–198.
[26] C. Dreszer, J.S. Vrouwenvelder, A.H. Paulitsch-Fuchs, A. Zwijnenburg, J.C. Kruithof, H.-C. Flemming, Hydraulic resistance of biofilms, J. Membr. Sci. 429 (2013) 436–447.
[27] W.J. Gao, H.J. Lin, K.T. Leung, H. Schraft, B.Q. Liao, Structure of cake layer in a submerged anaerobic membrane bioreactor, J. Membr. Sci. 374 (2011) 110–120.
[28] M. Hashino, T. Katagiri, N. Kubota, Y. Ohmukai, T. Maryuma, H. Matsyuyama, Effect of surface roughness of hollow fiber membranes with gear-shaped structure on membrane fouling by sodium alginate, J. Membr. Sci. 366 (2011) 389–397.